NANO LETTERS

pubs.acs.org/NanoLett Letter

# Observation of Surface Ligands-Controlled Etching of Palladium Nanocrystals

Qi Zheng, Junyi Shangguan, Xinle Li, Qiubo Zhang, Karen C. Bustillo, Lin-Wang Wang, Jinyang Jiang,* and Haimei Zheng*

Cite This: *Nano Lett.* 2021, 21, 6640−6647 Read Online

ACCESS | Metrics & More | Article Recommendations | Supporting Information

**ABSTRACT:** Selective adsorption of ligands on nanocrystal surfaces can affect oxidative etching. Here, we report the etching of palladium nanocrystals imaged using liquid cell transmission electron microscopy. The adsorption of surface ligands (i.e., iron acetylacetonate and its derivatives) and their role as inhibitor molecules on the etching process were investigated. Our observations revealed that the etching was dominated by the interplay between palladium facets and ligands and that the etching exhibited different pathways at different concentrations of ligands. At a low concentration of iron acetylacetonate (0.1 mM), rapid etching primarily at {100} facets led to a concave structure. At a high concentration (1.0 mM), the etch rate was decreased owing to a protective film of iron acetylacetonate on the {100} facets and a round nanoparticle was achieved. Ab initio calculations showed that the differences in adsorption energy of inhibitor molecules on palladium facets were responsible for the etching behavior.

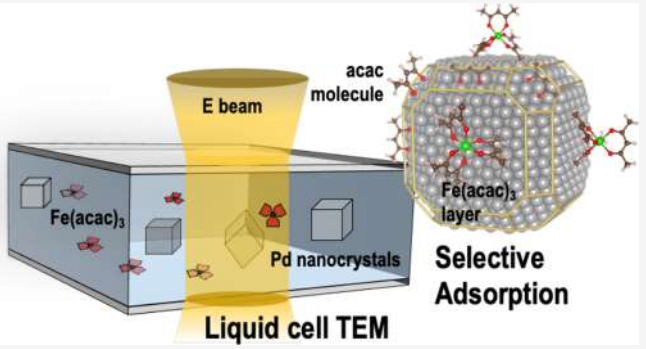


**KEYWORDS:** *Liquid cell, in situ transmission electron microscopy, etching, surface adsorption, ligand, inhibitor molecules*



The adsorption of ligand molecules on nanocrystal surfaces strongly influences the nanocrystal behavior in a variety range of applications, including catalysis,[1−3] self-assembly,[4−6] synthesis,[7−9] and etching.[10−14] Oxidative etching has emerged as a feasible approach to manipulate the shape of nanocrystals.[15] During the etching reactions, organic molecules or ions can be adsorbed on specific facets,[16−18] which lead to facet-dependent etching and formation of nanocrystals with various morphologies.[19−22] However, many specifics, such as the binding location of ligands and their effect on nanocrystal shape transformations, still warrant experimental observation.

The recent developments in liquid cell transmission electron microscopy (TEM)[23−27] have enabled direct imaging of chemical reactions in liquids, including nucleation,[28−30] growth,[31,32] self-assembly of nanocrystals,[33,34] and dynamic phenomena at electrode−electrolyte interfaces.[35,36] Liquid cell TEM has been used to address some scientific issues regarding ligands,[37−40] for example, surface ligands can impact the etching behavior,[41] while the adsorption sites of ligands on specific nanoparticle facets as well as the correlated etching dynamics has not been revealed.

Herein, we investigated the etching of ∼20 nm palladium (Pd) nanocrystals in an aqueous solution of $FeCl_3$ and iron(III) acetylacetonate ($Fe(acac)_3$). Typically, transition metal acetylacetonate is a promising candidate to inhibit etching,[42−44] and consequently, $Fe(acac)_3$ was used as the inhibitor molecule to control the etching of Pd nanocrystals. By taking advantage of *in situ* liquid cell TEM, we directly observed the etching of Pd nanocrystals by tracking the facet evolution. It is worth noting that since Pd nanocrystals are widely used in catalysis[45,46] and biosensing,[47] the stability of Pd nanocrystals in various environments is of great interest.[48−50] An understanding of the etching behavior of Pd nanocrystals described in this study may facilitate further practical applications.

To prepare a liquid cell sample for our *in situ* TEM experiment, a droplet of ∼2 μL reaction solution containing Pd nanocrystals, $FeCl_3$, and $Fe(acac)_3$ was encapsulated between two carbon films (Figure 1A, also see Methods). Note that the free $Fe^{3+}$ from $FeCl_3$ acted as the primary etchant[51] while the iron bonded in $Fe(acac)_3$ served as a coordination complex. Upon evaporating excess liquid, the liquid cell was sealed and subsequently transferred into the microscope for real-time imaging. We found that the Pd nanocrystals were uniformly distributed in the liquid cell (Figure 1B). The Pd nanocrystals

Received: May 29, 2021
Revised: July 25, 2021
Published: July 29, 2021

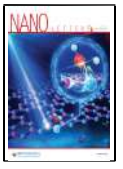




https://doi.org/10.1021/acs.nanolett.1c02104
*Nano Lett.* 2021, 21, 6640−6647

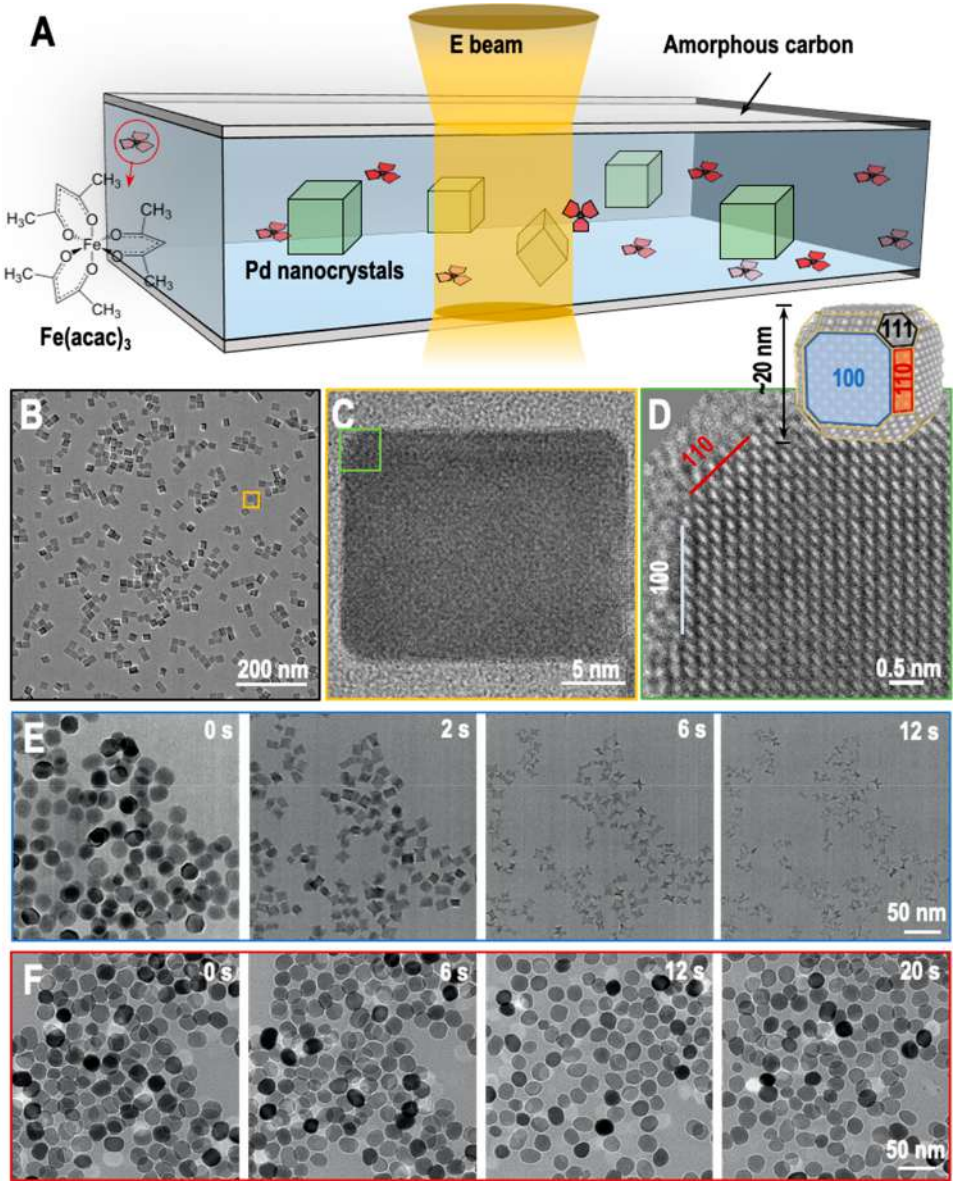


**Figure 1.** Etching of Pd nanocrystals at different $Fe(acac)_3$ concentrations. (A) A schematic setup of *in situ* liquid cell TEM experiment with Pd nanocrystals and $Fe(acac)_3$ in water. (B) A low-magnification TEM image of the Pd nanocrystals distributed in the liquid cell. (C) A single-crystalline Pd nanocrystal. (D) A high-resolution TEM image of a Pd nanocrystal. The (100) and (110) facets can be distinguished. (E) Rapid etching of Pd nanocrystals at 0.1 mM $Fe(acac)_3$. (F) Mitigated etching of Pd nanocrystals in the 1 mM $Fe(acac)_3$ aqueous solution.

had an average size of ~20 nm and exhibited a truncated cubic shape (Figure 1C, also see Figure S1) with exposed (100), (110), and (111) facets (Figure 1D). The three-dimensional view of the Pd nanocrystal was observed when it was rotating in the liquid cell (Figure S2).

Different etching phenomena were noticed at two different $Fe(acac)_3$ concentrations. At 0.1 mM $Fe(acac)_3$, a rapid etching of Pd nanocrystals was observed, as shown in Figure 1E. At this low concentration of $Fe(acac)_3$, most of the Pd nanocrystals showed etch completion after 12 s. However, the etching was significantly suppressed under a high $Fe(acac)_3$ (1.0 mM); no obvious shape change or little size change was observed after 20 s (Figure 1F). In both cases, some electron radiolysis species such as $O_2$ and $H_2O_2$ can promote the initial etching.[52] It seems that there was moderate etching at the corners of Pd nanocrystals at the initial stage ("0 s" refers to the initial imaging time). Note that the electron dose rate ($\sim 200\ e \cdot Å^{-2} \cdot s^{-1}$) was controlled in the same manner in Figure 1E,F to incorporate the same electron beam effect in both concentrations. These results indicate that $Fe(acac)_3$ molecules readily impacted the etching of Pd nanocrystals, leading to different etch rates and etching modes.

The individual Pd nanocrystal was traced with high resolution to quantify the nanocrystal shape evolution during etching. At the low $Fe(acac)_3$ concentration (0.1 mM), the etching reactions initiated at the {100} facets and proceeded rapidly along the ⟨100⟩ directions (Figure 2A). In this scenario, the fast etching along the ⟨100⟩ directions led to transforming the truncated Pd nanocube into a concave nanoparticle within 10 s. Meanwhile, we observed moderate etching at the corners. With continuous etching primarily along the ⟨100⟩ directions, the concave cube split into small fragments. Most Pd nanocrystals were dissolved after 16 s.


https://doi.org/10.1021/acs.nanolett.1c02104
Nano Lett. 2021, 21, 6640−6647

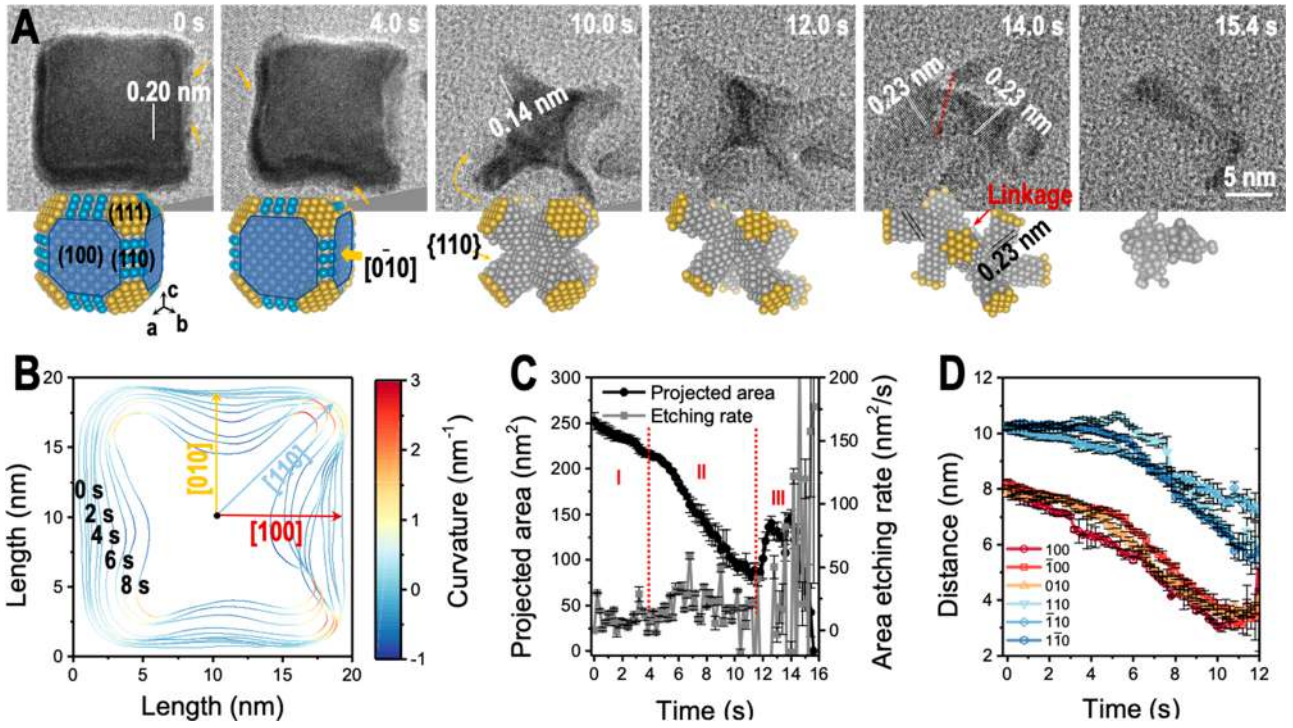


**Figure 2.** Rapid etching of a Pd nanocrystal at 0.1 mM $Fe(acac)_3$. (A) Time series of *in situ* TEM images (Supplementary Video 1) and corresponding schematics showing the shape evolution throughout the etching process. The {100} facets were highlighted in blue. (B) Time-domain contour plots of the Pd nanocrystal. Contour lines are spaced in time by 1 s. The color of the curves represents the local curvature. (C) Projected area and etch rate of Pd nanocrystal as a function of time. (D) The average center-to-face distance as a function of time. The average etching rates were calculated based on different time ranges. Error bars, standard deviation from multiple measurements.

To better understand the spatiotemporal details of the reaction, we constructed time-domain contour plots showing the dynamic shape evolution of the Pd nanocrystal, colored based on the local curvature. As shown in Figure 2B for the case of the low concentrated $Fe(acac)_3$ (0.1 mM), it reveals a unique etching mode dominated by the {100} facets with low curvature values. This is different from the commonly reported cases without inhibitor molecules[53] in which etching initiates in the location with high curvature due to the high surface energy at the low coordinated sites.[51,54,55] Our results can be attributed to the capping effect of inhibitor molecules on certain facets so that the selective oxidation of {100} facets leads to the formation of a concave structure. We classified the etching of the Pd nanocrystal into three stages based on the projected area etch rate, as shown in Figure 2C. Etching in the initial period was mild at the rate of ~6 nm$^2$/s, followed by a steady etching period at ~18 nm$^2$/s through etching of the {100} facets. The accelerated etching after ~4 s can be attributed to the increase of specific surface area with more low-coordinated atoms exposed because of the formation of concave structure. Finally, an acceleration period was noticed at a rate of ~22 nm$^2$/s once the concave structure collapsed. Etching of the Pd nanocrystal exhibited symmetrical characteristics concerning the evolution of center-to-face distance of the equivalent facets, such as the {100} and {110}, is similar (Figure 2D). This is governed by the geometry of Pd nanocube,[56] and it is consistent with the shape evolution as shown in Figure 2B.

At high $Fe(acac)_3$ concentration (1.0 mM), the etching of Pd was significantly mitigated by the presence of the ligands at the nanocrystal surfaces. Sequential TEM images and the contour maps show that the truncated Pd nanocube evolved into nearly a spherical nanoparticle after 8 s of etching (Figure 3A,B). A crystalline thin film on the nanocrystal surface was observed. The thin film hindered the etching of the Pd nanocrystal, especially the {100} facets. This layered structure was further determined to be $Fe(acac)_3$ based on the crystal structure imaged by high-resolution TEM and chemical EDS mapping (see more details in Figure 4 and Figure S5). In contrast to the initial etching at low $Fe(acac)_3$ concentration where etching starts from {100} facets, the {110} and {111} facets are active and etched in this case since they are mostly exposed to the etchant solution without the protecting film. Thus, the etching leads to the transition of the truncated Pd nanocube into a nearly spherical shape.

The etching kinetics was revealed in Figure 3C by showing that the projected area of Pd nanocrystal declined from 272 to 215 nm$^2$ while its circularity increased to 0.99 as a function of time. We calculated the circularity ($C$) using the formula: $C = 4\cdot\pi\cdot(\text{area}/\text{perimeter}^2)$. The rise in circularity represents the Pd nanocrystal transformation from highly faceted to almost a sphere. Figure 3D indicates that the etching was symmetric in 1.0 mM $Fe(acac)_3$ and that the etch rates at different facets were almost the same and equal to 0.16 nm/s.

We observed that at high electron dose rate (~2700 e·Å$^{-2}$·s$^{-1}$), the surface protective layer of $Fe(acac)_3$ crystal can be damaged resulting in an etching mode that was similar to the mode of the low concentration $Fe(acac)_3$ (Figure S3). We also discovered that the etch rate was faster than if the protective layer remained intact by a factor of 2 from ~0.9 to ~3 nm$^2$/s, at a higher electron dose rate of ~2700 e·Å$^{-2}$·s$^{-1}$ (Figure S4).

High-resolution images of the $Fe(acac)_3$ crystalline film on the Pd nanocrystals in a concentrated $Fe(acac)_3$ solution (1.0 mM) are shown in Figure 4A,B. The $Fe(acac)_3$ film shows a


https://doi.org/10.1021/acs.nanolett.1c02104
Nano Lett. 2021, 21, 6640−6647

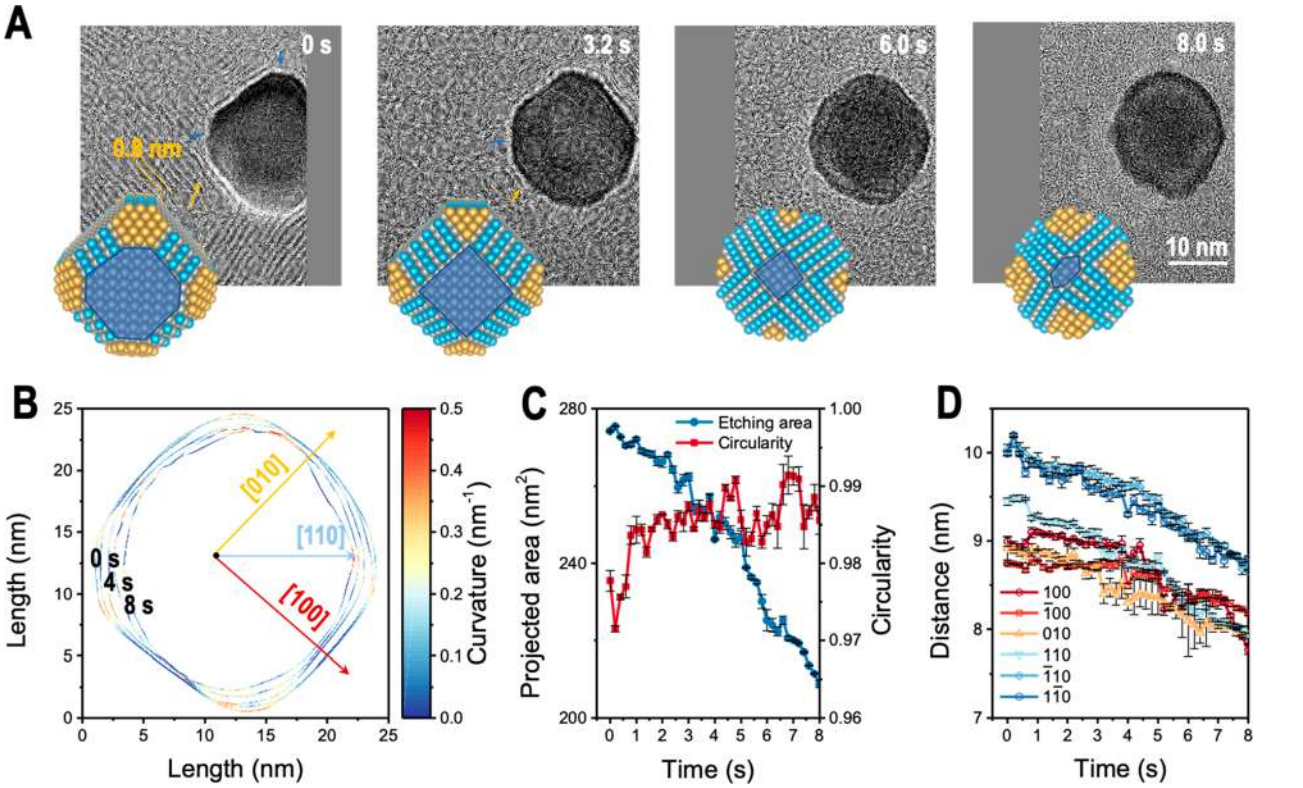


**Figure 3.** Mitigated etching of a Pd nanocrystal at 1.0 mM $Fe(acac)_3$. (A) Time series of *in situ* TEM images (Supplementary Video 2) with corresponding schematics during the shape evolution. The {100} facets are highlighted in blue. (B) Time-domain contour plots of the Pd nanocrystal. Contour lines are spaced in time by 2 s. The color of the curves shows the local curvature. (C) Projected area and circularity of the Pd nanocrystal as a function of time. (D) The average center-to-face distance as a function of time, extracted from contour plots in (B). The average etching rates were calculated based on different time ranges. Error bars, standard deviation from multiple measurements.

layered structure with a 0.85 nm spacing, which corresponds to the (100) spacing of the $Fe(acac)_3$ crystal (Figure 4C). Our characterization of the $Fe(acac)_3$ film is consistent with the reported $Fe(acac)_3$ crystal structure[57] in which the $Fe(acac)_3$ molecular layers are assembled by van der Waals force. The chemical maps of the film derived from STEM EDS data can be found in Figure S5. The $Fe(acac)_3$ film is only located on the {100} facets of Pd nanocrystals, which means localized protection.

$Fe(acac)_3$ can transform into free $Fe^{3+}$ and acetylacetonate (acac) molecules and vice versa in an aqueous solution. We employed UV−vis spectroscopy to identify the transition states of $Fe(acac)_3$ at different concentrations. In Figure 4D, the peaks at ∼450 and ∼350 nm are assigned to the absorbance of the coordination bonds between Fe and acac molecules, while the peak at ∼300 nm originates from the conjugated C═C bonding.[58] It shows that $Fe(acac)_3$ remains the coordination complex at 1.0 mM. However, $Fe(acac)_3$ dissociates into acac molecules at the concentration of 0.1 mM. This is consistent with the poor solubility of $Fe(acac)_3$ in water.[57]

The state of $Fe(acac)_3$ is dependent on its concentration. As shown in Scheme 1A, at a high concentration (1 mM), the coordinated $Fe(acac)_3$ dominates while at a low concentration (0.1 mM), the abundant species are acac molecules and dissociated $Fe^{3+}$ ions. Accordingly, the free $Fe^{3+}$ ions can enhance the etching of Pd through oxidation reactions. At high concentration, the primary species in solution is $Fe(acac)_3$ molecules. The interaction between the $Fe(acac)_3$ molecule and Pd substrate is van der Waals force (Scheme 1B), which is regarded as "physisorption".[59] We calculated the adsorption energies of $Fe(acac)_3$ on different Pd facets based on density functional theory (DFT). The results show that the differences in the absorption energy are minimal (Table 1). We consider that the $Fe(acac)_3$ molecules prefer to attach to the {100} facets because of the flat surface of the {100} facets and a good lattice match.[60] Both {100} facet of $Fe(acac)_3$ crystal and the {100} facet of Pd crystal share the orthogonal crystallographic symmetry, and similar *d*-spacings, which may facilitate the epitaxial growth of $Fe(acac)_3$ on Pd facets (Figure S6). These findings corroborate well with our experimental observations shown in Figure 4A.

In the low concentration case, the acac molecules are the primary products from $Fe(acac)_3$ dissociation. DFT calculations involving structure optimization show that covalent bonding between Pd adatom and the acac molecule is expected (Scheme 1C, also see Figure S7). The calculations suggest that the acac molecules are "chemisorbed" on the Pd surface in the 0.1 mM $Fe(acac)_3$.[61] The adsorption energy of acac molecule on Pd {110} is much lower than the adsorption energy on the Pd {100} facets, which indicates the molecule interacts more strongly with Pd atoms on the Pd {110} than on the {100}. The adsorption of acac molecules stabilizes the surface Pd {110} by forming the $Pd(acac)_2$ complex, resulting in the modified surface energy landscape.[62]

Dissociation occurs at both concentrations with acac molecules adsorbed on Pd facets. For example, at the high concentration of $Fe(acac)_3$, the adsorption of $Fe(acac)_3$ on the Pd facets is a dynamic process accommodated by the "physisorption" of $Fe(acac)_3$ and "chemisorption" of acac molecules simultaneously. This implies that the etching of Pd


https://doi.org/10.1021/acs.nanolett.1c02104
Nano Lett. 2021, 21, 6640−6647

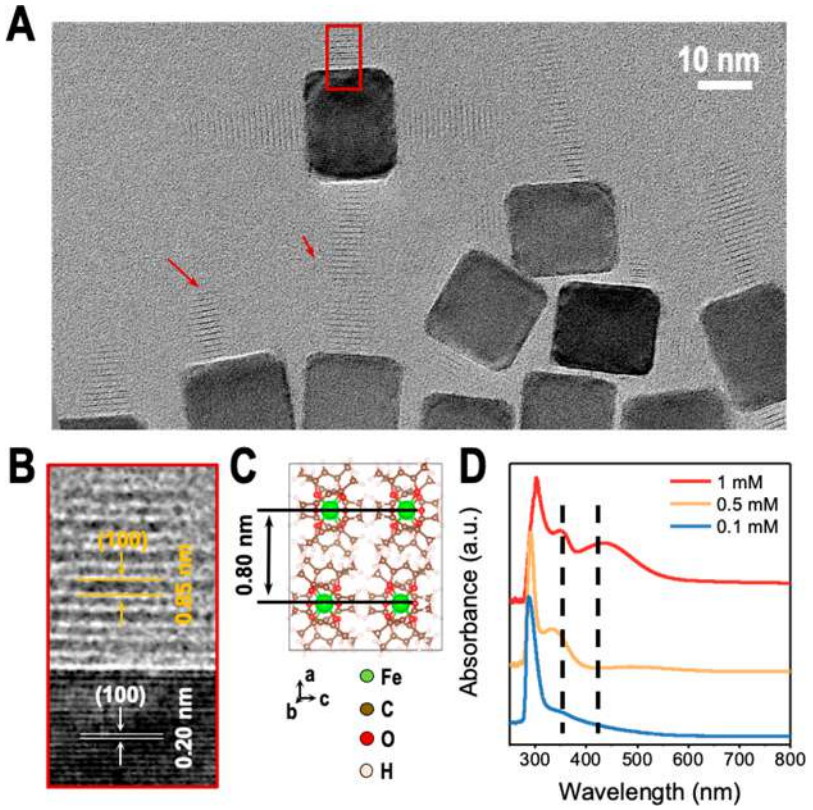


**Figure 4.** Distinct adsorption modes of $Fe(acac)_3$ on Pd facets at different concentrations. (A) A TEM image of $Fe(acac)_3$ molecular layers grown on the Pd (100) facet in the liquid cell at 1.0 mM $Fe(acac)_3$. (B) A high-resolution TEM image of the layered $Fe(acac)_3$ with a 0.85 nm interlayer distance. (C) Atomic structure of $Fe(acac)_3$ molecular crystal with consistent spacing. (D) UV−vis spectra of $Fe(acac)_3$ in solution at different concentrations. $Fe(acac)_3$ dissociates into acac molecules at 0.1 mM.

**Scheme 1. States of $Fe(acac)_3$ at Different Concentrations**[a]

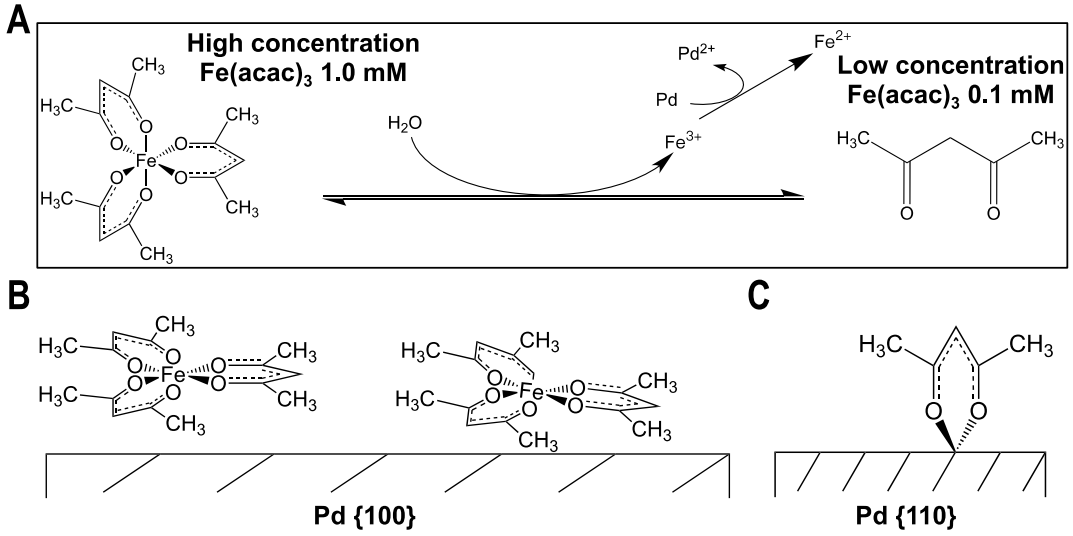


[a](A) $Fe(acac)_3$ can transform into free $Fe^{3+}$ and acetylacetonate (acac) molecules and vice versa, depending on the concentration. (B) The growth of $Fe(acac)_3$ molecular layers on the {100} facet at 1.0 mM $Fe(acac)_3$. (C) Adsorption of the acac molecule on the {110} facet at 0.1 mM $Fe(acac)_3$.

nanocrystals is mitigated by the physisorption of $Fe(acac)_3$ molecular film on the {100} facets and chemisorption of acac small molecules on the {110} facets. However, the protection by $Fe(acac)_3$ film is more effective with a thick layer up to ~10 nm. It is also noted that at the high concentration of $Fe(acac)_3$ (1 mM), the mitigation of etching can be dominated by the physical film protection of the {100} facets at the very beginning. If the $Fe(acac)_3$ film is destroyed by electron beam irradiation, the effects of acac molecules on the {110} facets are more prominent.

In summary, the nanoscale etching behavior of the Pd nanocrystals in the solution of $Fe(acac)_3$ was tracked in real-


https://doi.org/10.1021/acs.nanolett.1c02104
Nano Lett. 2021, 21, 6640−6647

**Table 1. Adsorption Energy of $Fe(acac)_3$ and acac on Pd Facets**

| | adsorption energy (eV) | |
|---|---|---|
| facet | $Fe(acac)_3$ | acac |
| (100) | −0.12 | −0.54 |
| (110) | −0.20 | −0.72 |
| (111) | −0.14 | −0.78 |

time through *in situ* liquid cell TEM. The facet-dependent etch rate, and the shape evolution of Pd nanocrystals were investigated at two different concentrations of $Fe(acac)_3$. At a low concentration of $Fe(acac)_3$ (0.1 mM), we found that the etching originated on the Pd {100} facets, while at a high concentration of $Fe(acac)_3$ (1.0 mM), the initial etching mostly occurs at the Pd {110} facets. At high concentrated $Fe(acac)_3$ (1.0 mM), an $Fe(acac)_3$ protective film was formed on the {100} facets, which significantly mitigated the etch rate of the {100} facets from 16 to 5 $nm^2/s$. *In situ* liquid cell TEM observation facilitates an opportunity to decipher nanoscale etching mechanisms and provides insights for designing corrosion-resistant nanomaterials by manipulating the interplay between inhibitor molecules and nanomaterials surfaces.

## METHODS

**Palladium Nanocrystals.** Pd nanocrystals were synthesized according to the reported method.[63] STEM imaging and energy dispersive spectroscopy (EDS) elemental mapping of the nanocrystals are shown in Figure S1. The concentration of Pd nanocrystals in solution was ∼40 μg/mL.

***In Situ* TEM.** The TEM liquid cell was prepared by encapsulating liquid between two carbon film-supported copper grids. First, the Pd nanocrystal solution was dropcasted on the carbon support on the first copper grid and air-dried for ∼5 min. Then, a droplet (∼2 μL) of the reaction solution (0.1 M $FeCl_3$, 0.2 mM HCl, and 0.1−1.0 mM $Fe(acac)_3$) was loaded onto the carbon support of the second copper grid and covered with the first grid. The liquid pockets were encapsulated between two carbon films supported on Cu grids due to van der Waals forces after evaporation of the excess liquid solution. Afterward, the liquid cell was loaded into an aberration-corrected transmission electron microscope for imaging. The *in situ* liquid cell experiments were performed on a Thermo Fisher Scientific ThemIS. The microscope was operated at 300 keV with a Super-X energy dispersive X-ray spectroscopy (EDS) detector, allowing for rapid chemical identification. The videos were recorded on a Ceta CMOS camera at 5 frames per second.

**UV−vis Spectroscopy.** The liquid-state UV−vis absorbance measurement was performed on Cary 5000 UV−vis-NIR spectrometer from 180 to 1000 nm with a step size of 1 nm.

**Density Functional Theory Calculations.** DFT calculations were performed by the Vienna Ab Initio Simulation Package (VASP).[64,65] The projector augmented wave (PAW) method[66,67] combined with the Perdew−Burke−Ernzerhof exchange[68] was used throughout the calculation. The plane-wave basis energy cutoff was set at 450 eV for high precision, and the related criteria were set $10^{-4}$ eV for total energy change and 0.02 eV/Å for the force on each atom. The Monkhorst−Pack grids in the Brillouin zone of the primitive cells were set 5 × 5 × 1 for k-point sampling.

The Pd(100), Pd(110), and Pd(111) surfaces were all modeled by periodically repeated unit cells. For example, the Pd(100) surface was achieved by a 3 × 3 supercell. Each slab consists of four Pd atomic layers; the bottom two layers were fixed at their bulk lattice positions while the top two layers and the adsorbates were allowed to relax fully. Successive slabs were separated in the *z*-direction by a vacuum layer of 25 Å.

The adsorption energy calculation formula is given below

$$E_{ads} = E_{adsorbate/surface} - E_{clean} - E_{adsorbate}$$

where $E_{adsorbate/surface}$, $E_{clean}$, and $E_{adsorbate}$ represent the total energies of the adsorbate-slab, the clean slab, and the adsorbate species, respectively.

## ASSOCIATED CONTENT

### Supporting Information

TThe Supporting Information is available free of charge at https://pubs.acs.org/doi/10.1021/acs.nanolett.1c02104.

Supporting figures and discussions; EDS mapping of Pd nanocrystals and electron beam effect (PDF)

Video 1 shows rapid etching of a Pd nanocrystal at 0.1 mM $Fe(acac)_3$ (AVI)

Video 2 shows mitigated etching of a Pd nanocrystal at 1.0 mM $Fe(acac)_3$ (AVI)

Video 3 shows electron beam damages the surface ligands with a different etching mode at 1.0 mM $Fe(acac)_3$ (AVI)

## AUTHOR INFORMATION


### Corresponding Authors

**Haimei Zheng** − *Materials Sciences Division, Lawrence Berkeley National Laboratory, Berkeley, California 94720, United States;* orcid.org/0000-0003-3813-4170; Email: hmzheng@lbl.gov

**Jinyang Jiang** − *School of Materials Science and Engineering, Southeast University, Nanjing 211189, P.R. China;* orcid.org/0000-0002-0134-9373; Email: jiangjinyang16@163.com

### Authors

**Qi Zheng** − *Materials Sciences Division, Lawrence Berkeley National Laboratory, Berkeley, California 94720, United States; School of Materials Science and Engineering, Southeast University, Nanjing 211189, P.R. China*

**Junyi Shangguan** − *Materials Sciences Division, Lawrence Berkeley National Laboratory, Berkeley, California 94720, United States*

**Xinle Li** − *Molecular Foundry, Lawrence Berkeley National Laboratory, Berkeley, California 94720, United States;* Present Address: (X.L.) Department of Chemistry, Clark Atlanta University, Atlanta, GA 30314, United States

**Qiubo Zhang** − *Materials Sciences Division, Lawrence Berkeley National Laboratory, Berkeley, California 94720, United States*

**Karen C. Bustillo** − *National Center for Electron Microscopy, Molecular Foundry, Lawrence Berkeley National Laboratory, Berkeley, California 94720, United States;* orcid.org/0000-0002-2096-6078

**Lin-Wang Wang** − *Materials Sciences Division, Lawrence Berkeley National Laboratory, Berkeley, California 94720, United States;* orcid.org/0000-0001-7061-2692

Complete contact information is available at: https://pubs.acs.org/10.1021/acs.nanolett.1c02104




https://doi.org/10.1021/acs.nanolett.1c02104
*Nano Lett.* 2021, 21, 6640−6647

### Notes

The authors declare no competing financial interest.

## ■ ACKNOWLEDGMENTS

This work was supported by the U.S. Department of Energy (DOE), Office of Science, Office of Basic Energy Sciences (BES), Materials Science and Engineering Division under Contract No. DE-AC02-05-CH11231 within the KC22ZH program. Work at the Molecular Foundry is supported by the Office of Science, Office of Basic Energy Sciences, of the U.S. Department of Energy under Contract No. DE-AC02-05CH11231. J.J. acknowledges the support from the National Natural Science Foundation of China (No. 51925903) and the National Key R&D Program of China (2018YFC0705401).

## ■ REFERENCES

(1) Chen, C.; Kang, Y.; Huo, Z.; Zhu, Z.; Huang, W.; Xin, H. L.; Snyder, J. D.; Li, D.; Herron, J. A.; Mavrikakis, M.; Chi, M.; More, K. L.; Li, Y.; Markovic, N. M.; Somorjai, G. A.; Yang, P.; Stamenkovic, V. R. Highly Crystalline Multimetallic Nanoframes with Three-Dimensional Electrocatalytic Surfaces. *Science* **2014**, *343* (6177), 1339−1343.

(2) Kuo, D.-Y.; Kawasaki, J. K.; Nelson, J. N.; Kloppenburg, J.; Hautier, G.; Shen, K. M.; Schlom, D. G.; Suntivich, J. Influence of Surface Adsorption on the Oxygen Evolution Reaction on $IrO_2$ (110). *J. Am. Chem. Soc.* **2017**, *139* (9), 3473−3479.

(3) Fu, Q.; Bao, X. Surface Chemistry and Catalysis Confined under Two-Dimensional Materials. *Chem. Soc. Rev.* **2017**, *46* (7), 1842−1874.

(4) Yu, M.; Bovet, N.; Satterley, C. J.; Bengio, S.; Lovelock, K. R. J.; Milligan, P. K.; Jones, R. G.; Woodruff, D. P.; Dhanak, V. True Nature of an Archetypal Self-Assembly System: Mobile Au-Thiolate Species on Au (111). *Phys. Rev. Lett.* **2006**, *97* (16), 166102.

(5) Otero, R.; Gallego, J. M.; de Parga, A. L. V.; Martin, N.; Miranda, R. Molecular Self-Assembly at Solid Surfaces. *Adv. Mater.* **2011**, *23* (44), 5148−5176.

(6) Sun, D.; Riley, A. E.; Cadby, A. J.; Richman, E. K.; Korlann, S. D.; Tolbert, S. H. Hexagonal Nanoporous Germanium through Surfactant-Driven Self-Assembly of Zintl Clusters. *Nature* **2006**, *441* (7097), 1126−1130.

(7) Sun, Y.; Xia, Y. Shape-Controlled Synthesis of Gold and Silver Nanoparticles. *Science* **2002**, *298* (5601), 2176−2179.

(8) Zhang, G.; Qi, P.; Wang, X.; Lu, Y.; Li, X.; Tu, R.; Bangsaruntip, S.; Mann, D.; Zhang, L.; Dai, H. Selective Etching of Metallic Carbon Nanotubes by Gas-Phase Reaction. *Science* **2006**, *314* (5801), 974−977.

(9) Zhao, M.; Xia, Y. Crystal-Phase and Surface-Structure Engineering of Ruthenium Nanocrystals. *Nat. Rev. Mater.* **2020**, *5* (6), 440−459.

(10) Renner, F. U.; Stierle, A.; Dosch, H.; Kolb, D. M.; Lee, T.-L.; Zegenhagen, J. Initial Corrosion Observed on the Atomic Scale. *Nature* **2006**, *439* (7077), 707−710.

(11) Lin, D.; Liu, Y.; Li, Y.; Li, Y.; Pei, A.; Xie, J.; Huang, W.; Cui, Y. Fast Galvanic Lithium Corrosion Involving a Kirkendall-Type Mechanism. *Nat. Chem.* **2019**, *11* (4), 382−389.

(12) Peng, J.; Chen, B.; Wang, Z.; Guo, J.; Wu, B.; Hao, S.; Zhang, Q.; Gu, L.; Zhou, Q.; Liu, Z.; Hong, S.; You, S.; Fu, A.; Shi, Z.; Xie, H.; Cao, D.; Lin, C.-J.; Fu, G.; Zheng, L.-S.; Jiang, Y.; Zheng, N. Surface Coordination Layer Passivates Oxidation of Copper. *Nature* **2020**, *586* (7829), 390−394.

(13) Boyle, D. T.; Huang, W.; Wang, H.; Li, Y.; Chen, H.; Yu, Z.; Zhang, W.; Bao, Z.; Cui, Y. Corrosion of Lithium Metal Anodes during Calendar Ageing and Its Microscopic Origins. *Nat. Energy* **2021**, *6*, 487−494.

(14) Hersbach, T. J. P.; Yanson, A. I.; Koper, M. T. M. Anisotropic Etching of Platinum Electrodes at the Onset of Cathodic Corrosion. *Nat. Commun.* **2016**, *7* (1), 1−7.

(15) Long, R.; Zhou, S.; Wiley, B. J.; Xiong, Y. Oxidative Etching for Controlled Synthesis of Metal Nanocrystals: Atomic Addition and Subtraction. *Chem. Soc. Rev.* **2014**, *43* (17), 6288−6310.

(16) Kesavan, D.; Gopiraman, M.; Sulochana, N. Green Inhibitors for Corrosion of Metals: A Review. *Chem. Sci. Rev. Lett.* **2012**, *1* (1), 1−8.

(17) Finšgar, M.; Jackson, J. Application of Corrosion Inhibitors for Steels in Acidic Media for the Oil and Gas Industry: A Review. *Corros. Sci.* **2014**, *86*, 17−41.

(18) Hamadi, L.; Mansouri, S.; Oulmi, K.; Kareche, A. The Use of Amino Acids as Corrosion Inhibitors for Metals: A Review. *Egypt. Egypt. J. Pet.* **2018**, *27* (4), 1157−1165.

(19) Zheng, Y.; Zeng, J.; Ruditskiy, A.; Liu, M.; Xia, Y. Oxidative Etching and Its Role in Manipulating the Nucleation and Growth of Noble-Metal Nanocrystals. *Chem. Mater.* **2014**, *26* (1), 22−33.

(20) Xie, S.; Lu, N.; Xie, Z.; Wang, J.; Kim, M. J.; Xia, Y. Synthesis of Pd-Rh Core−Frame Concave Nanocubes and Their Conversion to Rh Cubic Nanoframes by Selective Etching of the Pd Cores. *Angew. Chem.* **2012**, *124* (41), 10412−10416.

(21) Zhang, H.; Jin, M.; Wang, J.; Li, W.; Camargo, P. H. C.; Kim, M. J.; Yang, D.; Xie, Z.; Xia, Y. Synthesis of Pd− Pt Bimetallic Nanocrystals with a Concave Structure through a Bromide-Induced Galvanic Replacement Reaction. *J. Am. Chem. Soc.* **2011**, *133* (15), 6078−6089.

(22) Chen, M.; Wu, B.; Yang, J.; Zheng, N. Small Adsorbate-Assisted Shape Control of Pd and Pt Nanocrystals. *Adv. Mater.* **2012**, *24* (7), 862−879.

(23) Williamson, M. J.; Tromp, R. M.; Vereecken, P. M.; Hull, R.; Ross, F. M. Dynamic Microscopy of Nanoscale Cluster Growth at the Solid−Liquid Interface. *Nat. Mater.* **2003**, *2* (8), 532−536.

(24) Zheng, H.; Smith, R. K.; Jun, Y.; Kisielowski, C.; Dahmen, U.; Alivisatos, A. P. Observation of Single Colloidal Platinum Nanocrystal Growth Trajectories. *Science* **2009**, *324* (5932), 1309−1312.

(25) Liao, H.-G.; Cui, L.; Whitelam, S.; Zheng, H. Real-Time Imaging of Pt3Fe Nanorod Growth in Solution. *Science* **2012**, *336* (6084), 1011−1014.

(26) Yang, J.; Zeng, Z.; Kang, J.; Betzler, S.; Czarnik, C.; Zhang, X.; Ophus, C.; Yu, C.; Bustillo, K.; Pan, M.; Qiu, J.; Wang, L.-W.; Zheng, H. Formation of Two-Dimensional Transition Metal Oxide Nanosheets with Nanoparticles as Intermediates. *Nat. Mater.* **2019**, *18* (9), 970−976.

(27) de Jonge, N.; Houben, L.; Dunin-Borkowski, R. E.; Ross, F. M. Resolution and Aberration Correction in Liquid Cell Transmission Electron Microscopy. *Nat. Rev. Mater.* **2019**, *4* (1), 61−78.

(28) Smeets, P. J. M.; Cho, K. R.; Kempen, R. G. E.; Sommerdijk, N. A. J. M.; De Yoreo, J. J. Calcium Carbonate Nucleation Driven by Ion Binding in a Biomimetic Matrix Revealed by in Situ Electron Microscopy. *Nat. Mater.* **2015**, *14* (4), 394−399.

(29) Nielsen, M. H.; Aloni, S.; De Yoreo, J. J. In Situ TEM Imaging of CaCO3 Nucleation Reveals Coexistence of Direct and Indirect Pathways. *Science* **2014**, *345* (6201), 1158−1162.

(30) Liao, H.-G.; Zherebetskyy, D.; Xin, H.; Czarnik, C.; Ercius, P.; Elmlund, H.; Pan, M.; Wang, L.-W.; Zheng, H. Facet Development during Platinum Nanocube Growth. *Science* **2014**, *345* (6199), 916−919.

(31) Li, D.; Nielsen, M. H.; Lee, J. R. I.; Frandsen, C.; Banfield, J. F.; De Yoreo, J. J. Direction-Specific Interactions Control Crystal Growth by Oriented Attachment. *Science* **2012**, *336* (6084), 1014−1018.

(32) Liu, L.; Nakouzi, E.; Sushko, M. L.; Schenter, G. K.; Mundy, C. J.; Chun, J.; De Yoreo, J. J. Connecting Energetics to Dynamics in Particle Growth by Oriented Attachment Using Real-Time Observations. *Nat. Commun.* **2020**, *11* (1), 1−11.

(33) Luo, B.; Kim, A.; Smith, J. W.; Ou, Z.; Wu, Z.; Kim, J.; Chen, Q. Hierarchical Self-Assembly of 3D Lattices from Polydisperse Anisometric Colloids. *Nat. Commun.* **2019**, *10* (1), 1−9.

(34) Ou, Z.; Wang, Z.; Luo, B.; Luijten, E.; Chen, Q. Kinetic Pathways of Crystallization at the Nanoscale. *Nat. Mater.* **2020**, *19* (4), 450−455.



https://doi.org/10.1021/acs.nanolett.1c02104
*Nano Lett.* 2021, 21, 6640−6647

(35) Zeng, Z.; Zhang, X.; Bustillo, K.; Niu, K.; Gammer, C.; Xu, J.; Zheng, H. In Situ Study of Lithiation and Delithiation of $MoS_2$ Nanosheets Using Electrochemical Liquid Cell Transmission Electron Microscopy. *Nano Lett.* **2015**, *15* (8), 5214−5220.
(36) Lee, S.-Y.; Shangguan, J.; Alvarado, J.; Betzler, S.; Harris, S. J.; Doeff, M. M.; Zheng, H. Unveiling the Mechanisms of Lithium Dendrite Suppression by Cationic Polymer Film Induced Solid−Electrolyte Interphase Modification. *Energy Environ. Sci.* **2020**, *13* (6), 1832−1842.
(37) Kim, J.; Ou, Z.; Jones, M. R.; Song, X.; Chen, Q. Imaging the Polymerization of Multivalent Nanoparticles in Solution. *Nat. Commun.* **2017**, *8* (1), 1−10.
(38) Kim, J.; Jones, M. R.; Ou, Z.; Chen, Q. In Situ Electron Microscopy Imaging and Quantitative Structural Modulation of Nanoparticle Superlattices. *ACS Nano* **2016**, *10* (11), 9801−9808.
(39) Tan, S. F.; Chee, S. W.; Lin, G.; Mirsaidov, U. Direct Observation of Interactions between Nanoparticles and Nanoparticle Self-Assembly in Solution. *Acc. Chem. Res.* **2017**, *50* (6), 1303−1312.
(40) Anand, U.; Lu, J.; Loh, D.; Aabdin, Z.; Mirsaidov, U. Hydration Layer-Mediated Pairwise Interaction of Nanoparticles. *Nano Lett.* **2016**, *16* (1), 786−790.
(41) Hauwiller, M. R.; Ye, X.; Jones, M. R.; Chan, C. M.; Calvin, J. J.; Crook, M. F.; Zheng, H.; Alivisatos, A. P. Tracking the Effects of Ligands on Oxidative Etching of Gold Nanorods in Graphene Liquid Cell Electron Microscopy. *ACS Nano* **2020**, *14* (8), 10239−10250.
(42) Mahdavian, M.; Attar, M. M. Electrochemical Behaviour of Some Transition Metal Acetylacetonate Complexes as Corrosion Inhibitors for Mild Steel. *Corros. Sci.* **2009**, *51* (2), 409−414.
(43) Naderi, R.; Mahdavian, M.; Attar, M. M. Electrochemical Behavior of Organic and Inorganic Complexes of Zn (II) as Corrosion Inhibitors for Mild Steel: Solution Phase Study. *Electrochim. Acta* **2009**, *54* (27), 6892−6895.
(44) Tabatabaei majd, M.; Naderi, R.; Ramezanzadeh, B. Promotion of the Active/Barrier Protection Function of Epoxy Ester Coating/Steel System Utilizing Differently Synthesized Hybrid Pigment through Zinc Acetylacetonate Tailored with Green Inhibitor Molecules. *Prog. Org. Coat.* **2020**, *138*, 105380.
(45) Feng, Z.; Min, Q.-Q.; Fu, X.-P.; An, L.; Zhang, X. Chlorodifluoromethane-Triggered Formation of Difluoromethylated Arenes Catalysed by Palladium. *Nat. Chem.* **2017**, *9* (9), 918−923.
(46) Trost, B. M.; Min, C. Total Synthesis of Terpenes via Palladium-Catalysed Cyclization Strategy. *Nat. Chem.* **2020**, *12* (6), 568−573.
(47) Adam, V.; Hanustiak, P.; Krizkova, S.; Beklova, M.; Zehnalek, J.; Trnkova, L.; Horna, A.; Sures, B.; Kizek, R. Palladium Biosensor. *Electroanalysis* **2007**, *19* (18), 1909−1914.
(48) Sutter, E.; Jungjohann, K.; Bliznakov, S.; Courty, A.; Maisonhaute, E.; Tenney, S.; Sutter, P. In Situ Liquid-Cell Electron Microscopy of Silver−Palladium Galvanic Replacement Reactions on Silver Nanoparticles. *Nat. Commun.* **2014**, *5* (1), 1−9.
(49) Jiang, Y.; Zhu, G.; Lin, F.; Zhang, H.; Jin, C.; Yuan, J.; Yang, D.; Zhang, Z. In Situ Study of Oxidative Etching of Palladium Nanocrystals by Liquid Cell Electron Microscopy. *Nano Lett.* **2014**, *14* (7), 3761−3765.
(50) Chen, L.; Leonardi, A.; Chen, J.; Cao, M.; Li, N.; Su, D.; Zhang, Q.; Engel, M.; Ye, X. Imaging the Kinetics of Anisotropic Dissolution of Bimetallic Core−Shell Nanocubes Using Graphene Liquid Cells. *Nat. Commun.* **2020**, *11* (1), 1−10.
(51) Ye, X.; Jones, M. R.; Frechette, L. B.; Chen, Q.; Powers, A. S.; Ercius, P.; Dunn, G.; Rotskoff, G. M.; Nguyen, S. C.; Adiga, V. P.; Zettl, A.; Rabani, E.; Geissler, P. L.; Alivisatos, A. P. Single-Particle Mapping of Nonequilibrium Nanocrystal Transformations. *Science* **2016**, *354* (6314), 874−877.
(52) Schneider, N. M.; Norton, M. M.; Mendel, B. J.; Grogan, J. M.; Ross, F. M.; Bau, H. H. Electron−Water Interactions and Implications for Liquid Cell Electron Microscopy. *J. Phys. Chem. C* **2014**, *118* (38), 22373−22382.
(53) Gao, W.; Hou, Y.; Hood, Z. D.; Wang, X.; More, K.; Wu, R.; Xia, Y.; Pan, X.; Chi, M. Direct in Situ Observation and Analysis of the Formation of Palladium Nanocrystals with High-Index Facets. *Nano Lett.* **2018**, *18* (11), 7004−7013.
(54) Shan, H.; Gao, W.; Xiong, Y.; Shi, F.; Yan, Y.; Ma, Y.; Shang, W.; Tao, P.; Song, C.; Deng, T.; Zhang, H.; Yang, D.; Pan, X.; Wu, J. Nanoscale Kinetics of Asymmetrical Corrosion in Core-Shell Nanoparticles. *Nat. Commun.* **2018**, *9* (1), 1011.
(55) Hauwiller, M. R.; Frechette, L. B.; Jones, M. R.; Ondry, J. C.; Rotskoff, G. M.; Geissler, P.; Alivisatos, A. P. Unraveling Kinetically-Driven Mechanisms of Gold Nanocrystal Shape Transformations Using Graphene Liquid Cell Electron Microscopy. *Nano Lett.* **2018**, *18* (9), 5731−5737.
(56) Xia, Y.; Xia, X.; Peng, H.-C. Shape-Controlled Synthesis of Colloidal Metal Nanocrystals: Thermodynamic versus Kinetic Products. *J. Am. Chem. Soc.* **2015**, *137* (25), 7947−7966.
(57) Hu, M.-L.; Jin, Z.-M.; Miao, Q.; Fang, L.-P. Crystal Structure of Tris (AcetyIacetonato) Iron (III), $C_{15}H_{21}O_6Fe$, at 20 K. *Z. Kristallogr. - New Cryst. Struct.* **2001**, *216* (1−4), 631−632.
(58) Yin, X.; Shi, M.; Kwok, K. S.; Zhao, H.; Gray, D. L.; Bertke, J. A.; Yang, H. Dish-like Higher-Ordered Palladium Nanostructures through Metal Ion-Ligand Complexation. *Nano Res.* **2018**, *11* (6), 3442−3452.
(59) Bruch, L. W. Theory of Physisorption Interactions. *Surf. Sci.* **1983**, *125* (1), 194−217.
(60) Zur, A.; McGill, T. C. Lattice Match: An Application to Heteroepitaxy. *J. Appl. Phys.* **1984**, *55* (2), 378−386.
(61) Norsko, J. K. Chemisorption on Metal Surfaces. *Rep. Prog. Phys.* **1990**, *53* (10), 1253.
(62) Low, M. J. D. Kinetics of Chemisorption of Gases on Solids. *Chem. Rev.* **1960**, *60* (3), 267−312.
(63) Jin, M.; Liu, H.; Zhang, H.; Xie, Z.; Liu, J.; Xia, Y. Synthesis of Pd Nanocrystals Enclosed by {100} Facets and with Sizes< 10 nm for Application in CO Oxidation. *Nano Res.* **2011**, *4* (1), 83−91.
(64) Kresse, G.; Furthmüller, J. Efficient Iterative Schemes for Ab Initio Total-Energy Calculations Using a Plane-Wave Basis Set. *Phys. Rev. B: Condens. Matter Mater. Phys.* **1996**, *54* (16), 11169.
(65) Kresse, G.; Furthmüller, J. Efficiency of Ab-Initio Total Energy Calculations for Metals and Semiconductors Using a Plane-Wave Basis Set. *Comput. Mater. Sci.* **1996**, *6* (1), 15−50.
(66) Kresse, G.; Joubert, D. From Ultrasoft Pseudopotentials to the Projector Augmented-Wave Method. *Phys. Rev. B: Condens. Matter Mater. Phys.* **1999**, *59* (3), 1758−1775.
(67) Blöchl, P. E. Projector Augmented-Wave Method. *Phys. Rev. B: Condens. Matter Mater. Phys.* **1994**, *50* (24), 17953.
(68) Perdew, J. P.; Burke, K.; Ernzerhof, M. Generalized Gradient Approximation Made Simple. *Phys. Rev. Lett.* **1996**, *77* (18), 3865.


https://doi.org/10.1021/acs.nanolett.1c02104
*Nano Lett.* 2021, 21, 6640−6647